

# Towards Condition-Robust Palm Vein Recognition: Dataset and Performance Analysis

# Suhas Chate<sup>1</sup>, Vijay Patil<sup>2</sup>, Yuvraj Parkale<sup>3</sup>, Shailendrakumar Mukane<sup>4</sup>

<sup>1-4</sup>Department of Electronics and Telecommunication Engineering, SVPM's College of Engineering, Malegaon Bk, Savitribai Phule Pune University, Pune, Maharashtra, India.

E-mail: ¹suhas.chate@mit.asia, ²vvnnpp2002@gmail.com, ³yuvrajvparkale@gmail.com, ⁴smmukane18@gmail.com

#### **Abstract**

Palm vein biometrics is contactless identification through vascular vein patterns. The paper presents a new dataset of 500 palm vein images from 100 individuals in 5 conditions (normal, hot, cold, dusty, and lotion-applied). In contrast to current benchmarks, the dataset directly simulates environmental and physiological variations. It compares three feature-extraction pipelines (Kumar Gabor, IUWT-SAD and Maximum Curvature) to a proposed multi-feature ensemble SVM. The proposed SVM uses HOG, LBP and Gabor features. In all cases, the ensemble achieves a mean EER of 4.0 %, TAR FAR=10-3=72.3%, and AUC=0.963, which is on par with Kumar Gabor (EER 8.8%), MC (EER 13.1%), and IUWT-SAD (EER 16.4%). Performance is consistent in response to temperature changes. There is only slight performance deterioration in the presence of surface contaminants (dust, lotion). Calibration analysis indicates low error (ECE < 0.02, Brier < 0.03). A throughput of up to 12 images per second is achieved with the proposed feature pipeline. The results demonstrate that ensemble fusion is highly effective for condition-resilient palm vein recognition. The new dataset offers a good reference point for estimating real-world resilience beyond laboratory tests.

**Keywords:** Palm Vein Recognition, Biometrics, Vascular Patterns, Feature Extraction, Ensemble SVM, Contactless Authentication, Dataset Evaluation.

#### 1. Introduction

Biometric systems are v used for secure authentication and verification. In contrast to passwords or tokens that can be readily stolen, biometric systems work with inherent human physiological attributes that cannot be easily imitated [1]. Palm vein recognition is among the safest modalities because subcutaneous vascular patterns are internal and not contact with the environment [1],[2],[3],[4]. Near-infrared (NIR) light (700-900nm) assists in the improvement of vascular imaging by focusing on deoxygenated haemoglobin. Mode transmission systems have high contrast while mode reflection systems are cost-effective and suitable for use in ATMs [3]. Tri-spectral and polarized imaging increase the visibility of veins in all skin tones [5]. Palm vein identification, while promising, is vulnerable to temperature, dust, lotion, and light. Current databases like CASIA, PolyU, and VERA are useful for benchmarking but do not account for diversity in real-world capture conditions [6],[7]. Outdoor environments influence recognition performance [8]. Large models like vision transformers and large-kernel

networks achieve comparatively modest accuracy under changing conditions with minimal training [9]-[13].

#### 1.1 Palm Vein Biometrics

High-contrast vein shadows were provided by initial generation transmission systems [2], while reflection-mode applications were brought forth with NIR sensors and LEDs, e.g., Fujitsu PalmSecure (2003) [3]. Maximum Curvature (MC), Repeated Line Tracking (RLT), Local Binary Patterns (LBP), Weighted Local Descriptors (WLD) and 2D Gabor filters are utilized for feature extraction [4],[5]. Recent developments include free-posed capture, multispectral imaging, deep learning, and spoofing resistance [6], [8], [11], [14], [30]. IR vein legibility is sensitive to temperature, dust, lotion, humidity, and wind interaction [33], [34]. However, this is not experimentally verified. ROI consistency is sensitive to illumination, skin tone and sensor-hand distance sensitive [34], and wavelength optimization is still challenging [33], [35]. They are vulnerable to synthetic vein spoofing [53] and thermal drift [33]. Public databases (CASIA, PolyU, VERA) are limited to controlled setups. Deep learning methods [23]-[25] perform well on benchmarks but suffer under acquisition changes [11], [14].

# 1.2 Objectives

Despite progress in acquisition optimization robustness analysis in realistic conditions remains under-represented [3]. Available data sets do not adequately alter physiological and environmental factors [7]. The main tasks will address key problems in palm vein biometrics:

- Present a palm vein dataset with 500 samples from 100 subjects under five environmental conditions (normal, hot, cold, dusty, lotion) to capture variation.
- Compare preprocessing and ROI extraction techniques on feature extraction pipelines (Kumar Gabor, IUWT, Maximum Curvature) under the same conditions.
- Propose a multi-feature ensemble SVM classifier (HOG, LBP, Gabor descriptors).
   Test recognition accuracy, EER and TAR under different conditions to estimate environmental effects.

Section 2 overviews palm vein biometrics literature and places this research. Section 3 describes datasets, acquisition settings and subject populations. Section 4 describes the methodology-preprocessing, ROI extraction, features and matching. Section 5 presents experimental results and analysis, including baseline comparisons and robustness testing. Section 6 provides conclusions, limitations, and future research directions.

## 2. Related Works

The section presents the process utilized in palm vein feature-based human biometrics recognition. It also covers the work done by fellow researchers in the last decade across the globe.

#### 2.1 Imaging Principle

Palm vein patterns lie beneath the skin and require near-infrared (NIR) images for scanning. CD or CMOS-based ICs with NIR (850 nm) are applied [11]. Multispectral imaging shows high contrast between visible and invisible veins, independent of skin colour and physiological states [12]. Dual wavelength illumination at 760 nm and 940 nm provides higher contrast-to-noise ratios (CNR) [13]. Contact-based systems are more robust in pose and ROI matching than contactless approaches [14]. Motion blur, depth-of-field (DOF) and lighting affect contactless imaging. Solutions include VCSEL based NIR arrays [16] and polarization-selective meta-lenses [15]. Multispectral systems work better outdoors with QTS [17].

# 2.2 Preprocessing & ROI Extraction

Raw palm images are pre-processed into high contrast inputs for feature extraction. Previous methods used thresholding [11], while newer approaches use guidance filters [18] for vessel contrasting. Vessel enhancement methods like maximum curvature (MC), repeated line tracking (RLT) and Hessian-based approaches visualize vascular structures. ROI should be cropped using geometric landmarks to reduce pose variation [19]. Recent works use lightweight HRNet architectures [14] with key-point detection for accurate ROI localization despite rotations and background clutter.

#### 2.3 Handcrafted Feature Methods

Palm vein recognition used manual feature extractors before deep learning. Local textures were captured using HOG, LBP, and LPQ [20]. Gabor filters provided multiscale representations [21]. Wavelet techniques improved performance in low-quality imaging. Hybrid approaches combining texture descriptors with vein extraction showed better robustness [22]. However, handcrafted features require adjustments and lack cross-device generalization. CNNs from ResNet and EfficientNet outperform handcrafted features [23]. Vision Transformers model dependencies [25], while large-kernel CNNs improve structure capture [24]. Recent research uses state-space models [28] and neural architecture search [27]. StarMix improves generalization [29]. PVTree generates vascular topologies [30], while GANs produce high-fidelity images [31]. Palm veins can be spoofed by printed attacks. PAD uses physiological markers and multi-wavelength imaging [32]. Key datasets include CASIA, PolyU, VERA, PUT, TJU-PV and UC3M. Dataset differences affect cross-dataset performance. Evaluations use EER, accuracy, FAR, FRR, and ROC curves. Table 1 shows results.

**Table 1.** Representative Palm Vein Recognition Methods and Reported Performance

Method & Year	Feature Extraction / Model	Dataset(s)	EER (%)	Accuracy (%)
LBP, SLBP, MSLBP with LDA (2022) [20]	LBP, SLBP, MSLBP with LDABP	PolyU Multispectral Palmprint DB	-	Up to 99.96 (Blue

				spectrum, MSLBP)
VGG-16 + attention, multi- task loss (2022) [21]	VGG-16 + attention, multi-task loss	Infrared palm- vein datasets	-	98.89
Modal correlation fusion (purification + PLS + weighted sum) (2024) [22]	Hybrid handcrafted	Multimodal palmprint + palm vein	0.0173 - 0.0008	-
ResNet50 FT (2020) [23]	CNN TL	VERA, PolyU	0.6	98.4
LaKNet + StarMix (2023) [24], [29]	Large-kernel CNN + Aug	PUT, TJU-PV	0.42	99
Swin Transformer (2023) [25]	ViT	UC3M, PolyU	0.38	99.1
PVTree + ViT (2024) [30]	Synthetic pretrain + ViT	CASIA, PUT	0.36	99.3
Dual-WL + PAD CNN (2024) [32]	Liveness CNN	Custom	0.5	98.7

#### 3. Dataset

To evaluate palm vein recognition under real-world variability, a new dataset using a custom-built NIR device was developed. The dataset details and setup are given in [33], with attention to acquisition protocol, subject diversity, and environmental conditions.

#### 3.1 Acquisition Protocol

Each subject participated in an acquisition session conducted on different days to capture both short-term and medium-term variability. During each session, the subject's palm was imaged under five distinct conditions:

- 1. Normal Standard room temperature, clean palm.
- 2. Cold Palm cooled by contact with cold water for ~1 minute.
- 3. Hot Palm warmed with a heating pad or hot water exposure for  $\sim$ 1 minute.
- 4. Dusty Fine dust particles applied to simulate environmental contamination.
- 5. Lotion applied A thin layer of moisturizer applied to simulate oily or sweaty palms.

The acquisition environment was a controlled laboratory room at 24–26 °C with low ambient light. The custom enclosure minimized external light and maintained a palm-sensor distance of 22 cm. Subjects placed their palms on a guide surface to reduce motion blur during capture. Each palm was imaged once per condition, with 5 images per subject.

## 3.2 Subject Diversity

The dataset included 100 participants, consisting of 49 males and 51 females. All subjects were within the age range of 18 to 20 years. In terms of skin tone distribution, approximately 35% had light skin, 45% had medium skin, and 20% had dark skin. The participants were drawn entirely from the student population. Each condition includes 100 samples, providing a balanced evaluation of algorithms under environmental variations. Collected in a single session, the dataset captures short-term physiological dynamics and external perturbations (temperature shifts, surface contamination) critical for robustness analysis. A binomial estimate confirms that 100 samples per condition achieve >80% statistical power for detecting moderate TAR differences at FAR=10<sup>-3</sup>. However, when specifically evaluating the ability to detect a 2-percentage-point TAR improvement at FAR =  $10^{-3}$  with 95% confidence, the power is much lower. With only 100 samples per condition, the calculated statistical power remains below 10% across all five conditions (Normal, Hot, Cold, Dusty, Lotion). This indicates that while the dataset is sufficient to capture moderate differences, it is underpowered for detecting very small ( $\leq 2$  pp) TAR shifts. This limitation highlights the need for larger-scale datasets in future work. Limitations include the narrow age range (18–20 years) and absence of long-term variations (aging, sensor drift). Future work will incorporate crossdataset validation with public benchmarks (PolyU, VERA) to assess generalization. Images follow the format userno conditionno.jpg (e.g., 2 1.jpg). Example samples are shown in Fig. 1. The dataset will be released for non-commercial research upon request.

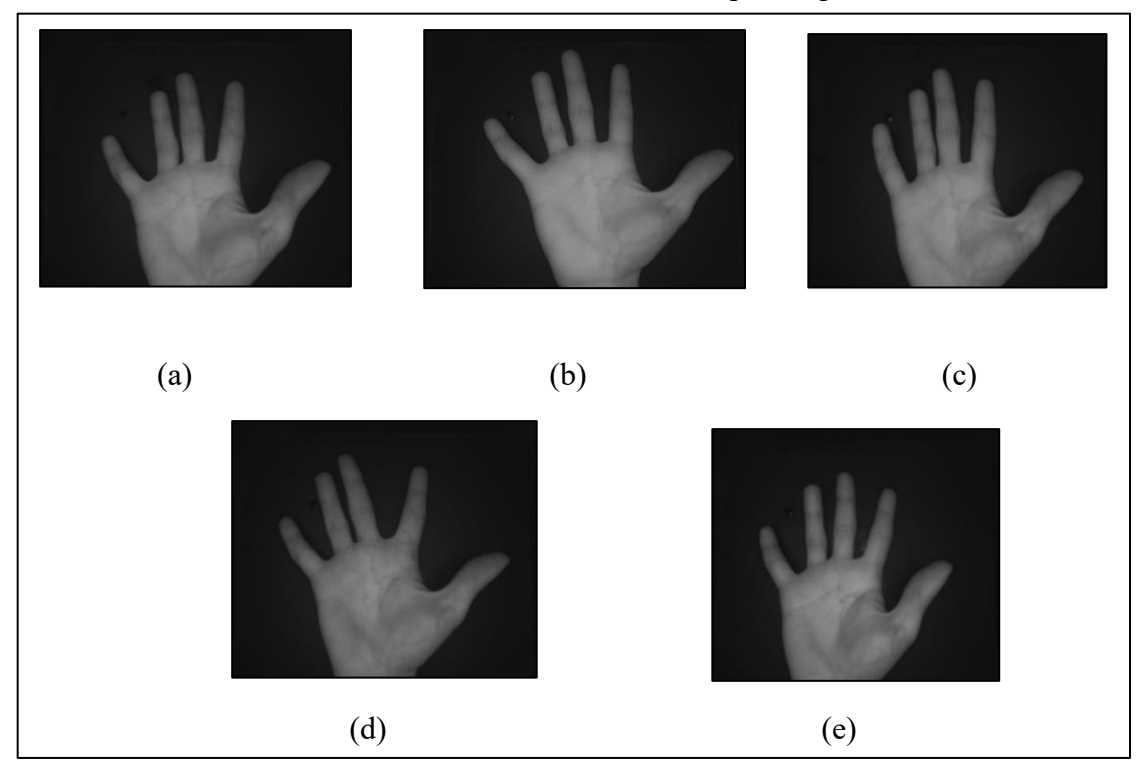


Figure 1. Palm Vein Images under Different Conditions: (a) Normal, (b) Cold Palm, (c) Hot Palm, (d) Dusty Palm and (e) Palm with Lotion

#### 4. Methodology

The PLUS OpenVein Toolkit is used to analyze the palm vein dataset [37]. It is an open-source MATLAB based implementation of various algorithms for examining blood vessel patterns. Additionally, an SVM classifier with a handcrafted multi-feature ensemble is proposed and employed. Three different methods, each with a unique matching technique, to identify features are employed.

# 4.1 Preprocessing and Region of Interest Localization (ROI)

The preprocessing pipeline features Otsu-based segmentation, adaptive-valley-point ROI detection, reflection correction, and Contrast Limited Adaptive Histogram Equalization (CLAHE).

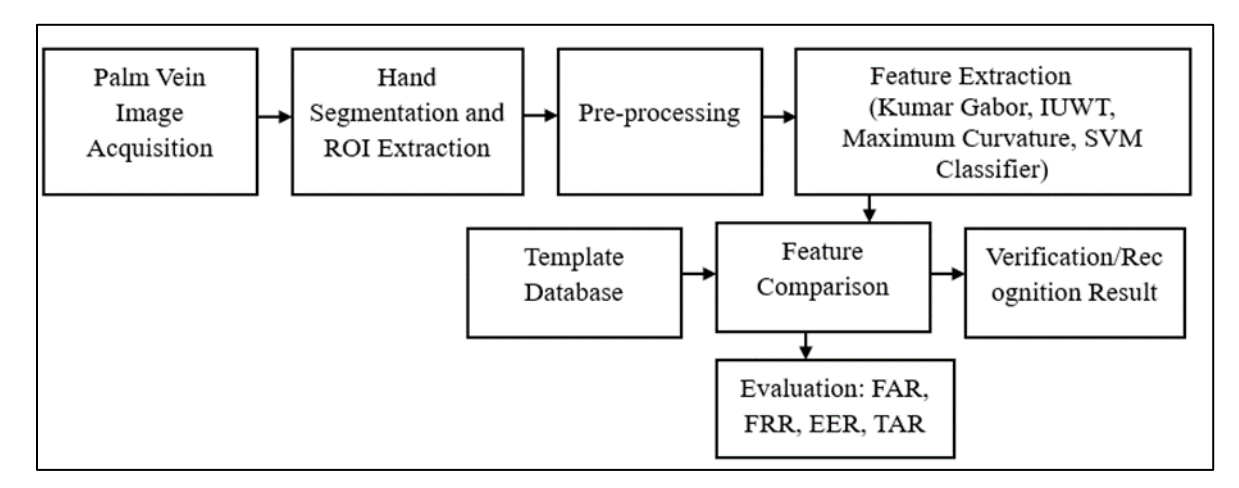


Figure 2. Overall Process Flow of the Proposed Palm Vein Recognition System

Preprocessing remained constant across all feature extractors (Gabor-NCC, IUWT-SAD, MC, and ensemble SVM) to minimize variability bias. Comparing CLAHE against raw normalization and standard Histogram Equalization (HE) showed that CLAHE maintained subtle vasculature and increased local contrast while avoiding noise issues during environmental changes. This work focused on system robustness under realistic physiological and environmental variability, without conducting complete ablation studies of individual preprocessing steps. Future work will analyze the contribution of each preprocessing stage to recognition accuracy. The overall workflow is summarized in Figure 2. Accurately identifying the palm's main vein-rich area is crucial, as it makes it easier to omit the fingers, wrist, and background. In this study, the region of interest (ROI) is identified using a technique based on the PalmNet framework [38].

# 4.1.1 Hand Segmentation

The input which is 2D image I(x, y) is converted to grayscale (if needed) and binarized via Otsu thresholding to produce a binary mask  $T_{Otsu}(x, y)$  of the hand region:

$$M_{Otsu}(x,y) = \begin{cases} 1, & I(x,y) \ge T_{Otsu}(x,y) \\ 0, & otherwise \end{cases}$$
 (1)

Figure 3 shows the thresholding process as given in equation (1).

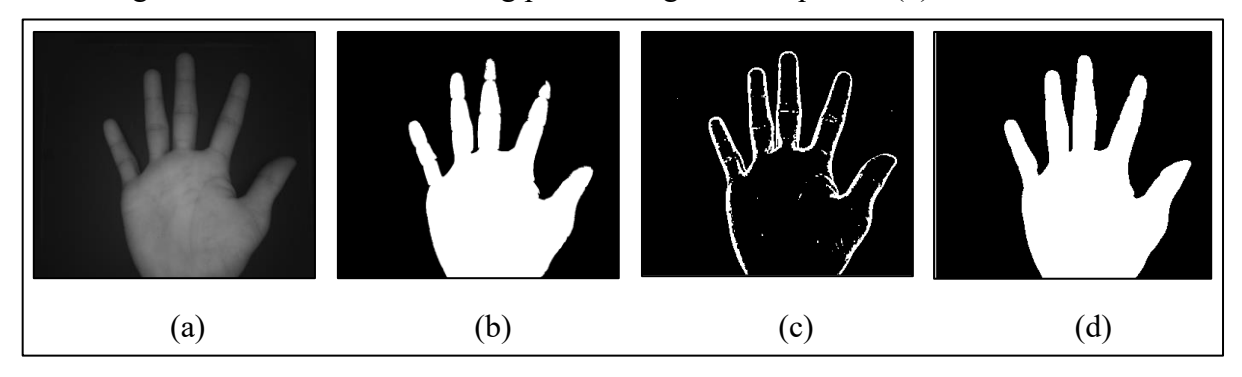


**Figure 3.** Palm Vein Image (a) Original (b) Threshold Image (c) Edge (d) Combined Image

A gradient-based edge map  $E_{add}(x, y)$  (Canny/Sobel) is computed. This detects missing boundary segments, particularly around finger edges where illumination or skin contrast is low. This is combined with the Otsu mask:

$$M_1 = M_{Otsu} \cup E_{add} \tag{2}$$

Figure 3 (c), (d) show the output of equation (2).

A second edge map  $E_{rem}(x, y)$  is generated. This helps identify spurious edges in the background or within the palm area (e.g., caused by noise or background objects). This is subtracted from the mask:

$$M_2 = M_1 - E_{rem} \tag{3}$$

Figure 4 shows the output of equation (3) where the edge map is subtracted from the binary image produced earlier. Morphological opening and closing refine  $M_2$ . this by reducing small objects and smoothing edges. High-intensity reflections in NIR images caused by skin specular highlights are identified via intensity thresholding:

$$R(x,y) = \begin{cases} 1, & I(x,y) \ge T_{refl} \\ 0, & otherwise \end{cases}$$
 (4)

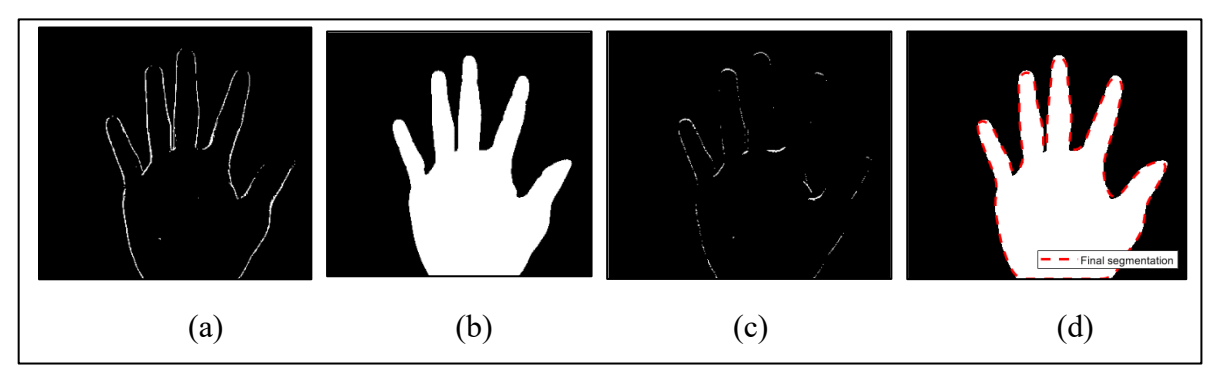


**Figure 4.** Palm Vein Image (a) Spurious Edge (b) Binary Palm (c) Reflection Regions (d) Final Binary Palm with Contour in Red Line

These reflection regions are re-added to the binary mask to restore missing fingertip or palm-edge pixels:

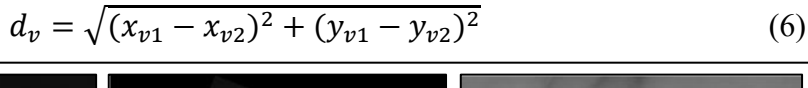
$$M_{final} = M_2 \cup R \tag{5}$$

Figure 4 (c), and (d) show the output of equation (4) and (5).

The result  $M_{final}$  is a noise-free, reflection-corrected hand mask. It accurately represents the palm boundary for subsequent ROI localization.

# 4.1.2 Adaptive Valley-Based ROI Localization

Valley point detection identifies two anatomical landmarks between the fingers. The Euclidean distance  $d_v$  between these points defines the ROI scale:



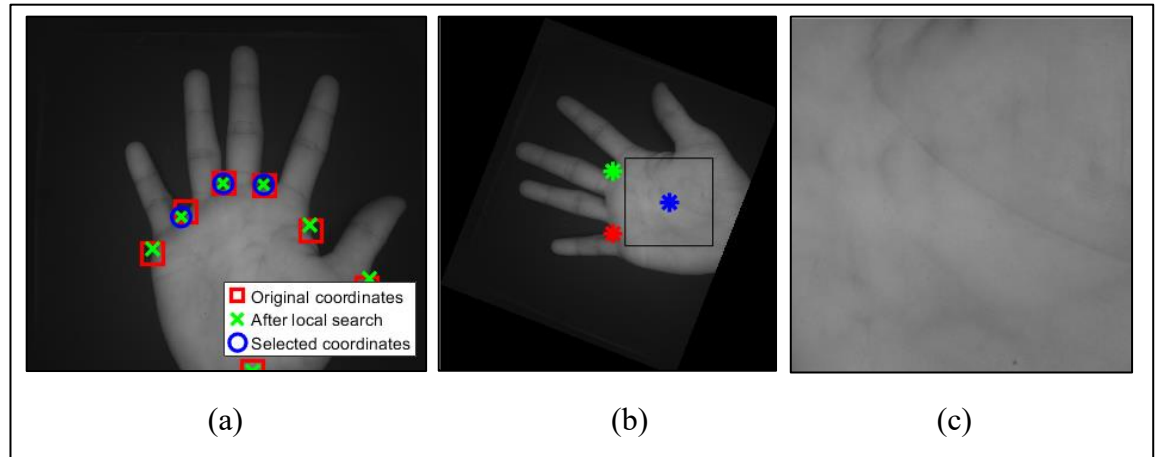


**Figure 5.** Palm Vein Image (a) Valley Points Detected (b) Rotated Image (c) Extracted ROI

ROI dimensions  $(w_{ROI}, h_{ROI})$  are set proportionally to  $d_v$ . The hand mask is rotated so its principal axis is vertically aligned:

$$I_r = R(I, -\theta), \theta = \frac{1}{2} \tan^{-1} \left( \frac{2\mu_{11}}{\mu_{20} - \mu_{02}} \right)$$
 (7)

The term  $\mu_{pq}$  refers to a central moment of order p+q of the binary hand mask (or grayscale image). p and q are the moment orders in x and y directions.  $\mu_{11}$  mixed second-order central moment, captures the correlation between x and y coordinates.  $\mu_{20}$  and  $\mu_{02}$  are second-order central moments along x and y axes respectively, representing spread in those directions. A square ROI centered at the palm centroid  $(x_c, y_c)$  is then extracted from  $I_r$ . Figure 5 shows the identified valley and reference points, the rotated palm with centroid and ROI mapped, and the final cropped ROI.

## 4.2 Preprocessing: Contrast Limited Adaptive Histogram Equalization (CLAHE)

CLAHE improves the visibility of low-contrast vein patterns in palm vein imaging by addressing the problem of uneven NIR lighting brought on by the palm's curvature and variations in skin scattering. A uniform distribution is used for CLAHE.

#### 4.3 Feature Extraction

Three different methods are used to analyse palm vein images. Each method comes from a different type of image analysis. A new algorithm is presented and tested with the dataset.

#### 4.3.1 Gabor Filtering

Gabor filters are spatial-frequency filters that achieve optimal joint localization in both spatial and frequency domains. These filters are extensively used in palm vein recognition to enhance oriented texture patterns, especially the vein ridges, by convolving the image with bandpass kernels that are specific to orientation and scale. The 2D Gabor filter is described as:

$$g(x, y; \lambda, \theta, \psi, \sigma, \Upsilon) = \exp\left(-\frac{x'^2 + \Upsilon^2 x y'^2}{2\sigma^2}\right) \cos\left(2\pi \frac{x'}{\lambda} + \psi\right)$$
(8)

Where  $x' = x\cos\theta + y\sin\theta$ ,  $y' = -x\sin\theta + y\cos\theta$ ,  $\lambda =$  wavelength of the sinusoidal factor (related to scale),  $\theta =$  filter orientation,  $\psi =$  phase offset,  $\sigma =$  Gaussian envelope's standard deviation,  $\gamma =$  spatial aspect ratio.

Kumar et al. [39] presented an improved multi-orientation Gabor filter design for hand vein imaging that can also be used for palm vein patterns.

$$R_{max}(x,y) = \max_{\theta \in \Theta} \sqrt{(I * g_{\theta}^{even})^2 + (I * g_{\theta}^{odd})^2}$$
 (9)

This method suppresses isotropic noise while improving linear vein structures. Background variations are suppressed by the Gaussian envelope. Regardless of hand posture, vessels are captured by the multi-orientation design. Vein continuity detection is improved by the phase congruency approach. The results of the Kumar Gabor approach's processing are displayed in Figure 6.

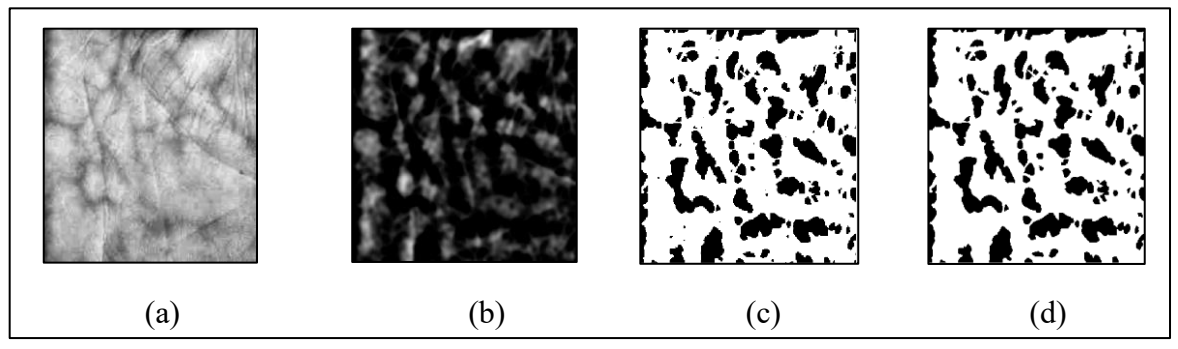


**Figure 6.** Palm Vein Processed ROI with Kumar Gabor Approach: (a) Normalized Image, (b) Accumulated Gabor Response, (c) Threshold Image and (d) Final Extracted Vein Pattern

# 4.3.2 Isotropic Undecimated Wavelet Transform (IUWT) for Palm Vein Feature Extraction

The Isotropic Undecimated Wavelet Transform (IUWT) is a type of wavelet transform. It works well for finding faint, line-like patterns, like palm veins. Unlike regular wavelet transforms, IUWT does not reduce the image size, so the image quality remains the same at all levels. Given an input image I(x, y), the IUWT decomposes it into a set of detail sub-bands  $w_i(x, y)$  at different scales j, and a coarse residual  $c_I(x, y)$  at the coarsest scale J:

$$I(x,y) = c_I(x,y) + \sum_{j=1}^{J} w_j(x,y)$$
 (10)

IUWT is applied to NIR palm images to produce multi-scale vein feature maps: Fine scales  $w_1$ ,  $w_2$  capture thin veins. Medium scales  $w_3$ ,  $w_4$  enhance main vascular trunks. The weighted reconstruction method reduces background texture but retains vein patterns. A binary vein map was created by setting a threshold on the sum of chosen detail coefficients.

$$S(x,y) = \sum_{j \in J} w_j(x,y)$$
 (11)

$$V_{map}(x,y) = \begin{cases} 1, & S(x,y) \ge T \\ 0, & otherwise \end{cases}$$
 (12)

where S is the set of relevant scales and T is an empirically chosen threshold. It avoids problems with aliasing and phase distortion because it does not reduce data. It keeps small details important for low-intensity veins. It can handle changes in rotation and position in contactless palm imaging. Figure 7 shows the result of the IWUT method.

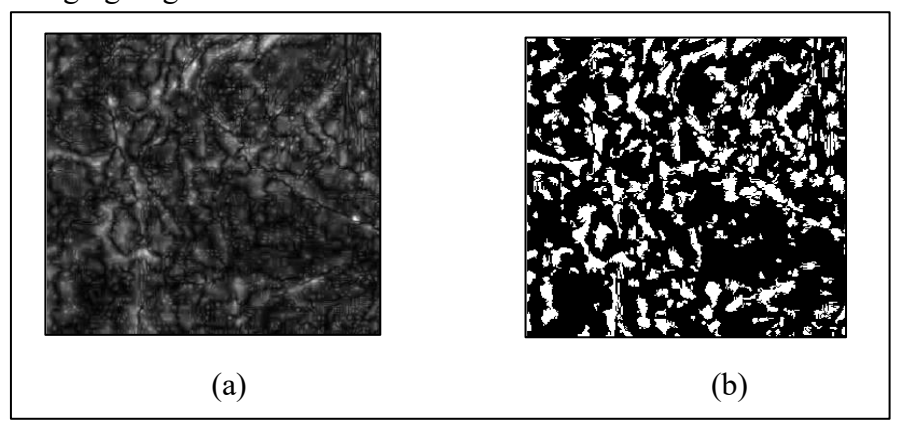


**Figure 7.** Palm Vein Processed ROI Applied with IUWT Approach: (a) IUWT Response (0 rotation), (b) Extracted Vein Pattern

# 4.3.3 Maximum Curvature (MC) Method

The Maximum Curvature (MC) method is a tool for finding the centreline of blood vessels. The MC method finds these lines by checking the curvature along different directions. If I(x, y) denote the preprocessed NIR palm image. For each scan line (row or column), the image intensity can be treated as a one-dimensional profile I(s) where s represents the position along the scan direction. The curvature is defined as.

$$k(s) = \frac{l''(s)}{[1 + (l'(s))^2]^{3/2}}$$
 (13)

Where I'(s) is the first order partial derivative and I''(s) is second order partial derivative. First zero-crossings of I'(s) where the slope changes from negative to positive (local minima) are identified (valley point). At each candidate valley point, k(s) is computed. Points with  $k(s) \ge T_c$  are considered as part of a vein centreline, where  $T_c$  is an empirically determined curvature threshold. The method is applied in both horizontal and vertical directions to capture veins running in multiple orientations.

$$V_{MC}(x,y) = V_{horizontal}(x,y) \cup V_{vertical}(x,y)$$
(14)

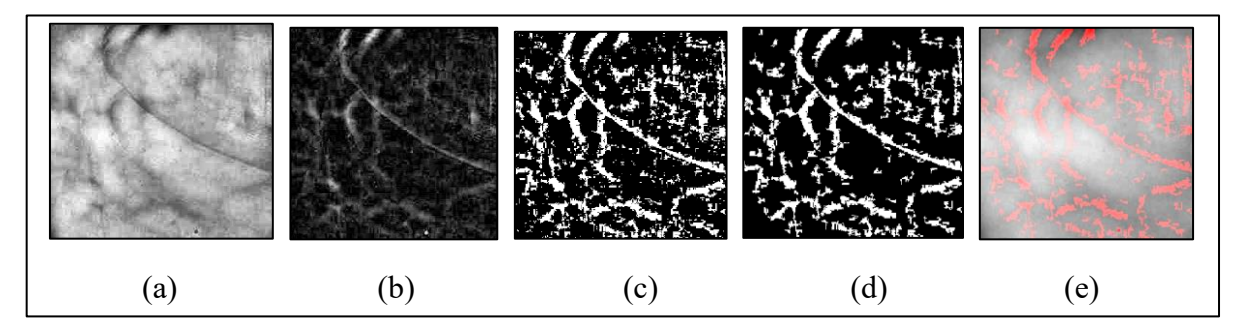


**Figure 8.** Palm Vein Processed ROI Applied with Maximum Curvature (a) Z-Normalized (b) Max Fused Response (c) Hybrid Threshold (d) Binary Vein Map (e) Palm Vein Overlapped on Original ROI

Figure 8 shows output of Maximum Curvature method.

#### 4.3.4 Handcrafted Multi-Feature Ensemble with SVM Classification

It begins with feature extraction using custom methods, followed by Support Vector Machine (SVM) classification. To capture palm vein characteristics like texture, edges, and frequency, this method combines various techniques. Images are resized for uniformity. CLAHE increases contrast to address lighting issues without increasing noise. Gaussian smoothing reduces high-frequency noise, while the Sobel operator highlights vein structures. Z-score normalization standardizes feature vectors before classification. Three handcrafted features are calculated per image. Histograms of Oriented Gradients (HOG) captures edge directions through gradient histograms in small areas. For a pre-processed ROI, horizontal and vertical gradients are computed using discrete derivative masks (Sobel operator).

$$G_{x} = I(x+1, y) - I(x-1, y)$$
(15)

$$G_{v} = I(x, y + 1) - I(x, y - 1)$$
(16)

The magnitude and orientation of each pixel's gradient are then:

$$m(x,y) = \sqrt{G_x^2 + G_y^2}, \ \theta(x,y) = \arctan(G_y, G_x)$$
 (17)

The ROI is divided into cells where gradient orientation histograms are computed with bins for evenly spaced angles (0°–180°). Each gradient contributes weighted by magnitude. Multi-scale HOG features are extracted using cell sizes of 8, 16×16, and 32×32 pixels to encode vascular structures. Local Binary Patterns (LBP) encode texture by thresholding pixel

intensities against the neighborhood mean, providing a rotation- and illumination-robust representation of vein structures. For a given pixel at  $(x_c, y_c)$  with intensity  $I_c$  and P neighbours on a circle of radius R, the LBP code is

$$LBP_{P,R}(x_c, y_c) = \sum_{p=0}^{P} s(I_p - I_c). 2^p$$
 (18)

where  $I_p$  is the intensity of the p-th neighbour and

$$s(z) = \begin{cases} 1, z \ge 0 \\ 0, z < 0 \end{cases} \tag{19}$$

In uniform patterns with up to two bitwise transitions, the histogram effectively differentiates features. Gabor filters ( $\lambda$ =4,8 pixels;  $\theta$ =0°,45°,90°,135°) extract orientation-specific frequency data. Each filter's mean and standard deviation statistically represent vascular patterns. The hybrid vector merges HOG, LBP, and Gabor features. Training images undergo random rotations ( $\pm$ 5°), translations ( $\pm$ 3 pixels), and contrast adjustments, applied to training samples only. Linear SVMs are trained for each descriptor, combining predictions via majority voting. For 0% recognition rates, a fallback nearest-neighbour match in hybrid space is triggered. Figure 9 shows classifier steps.

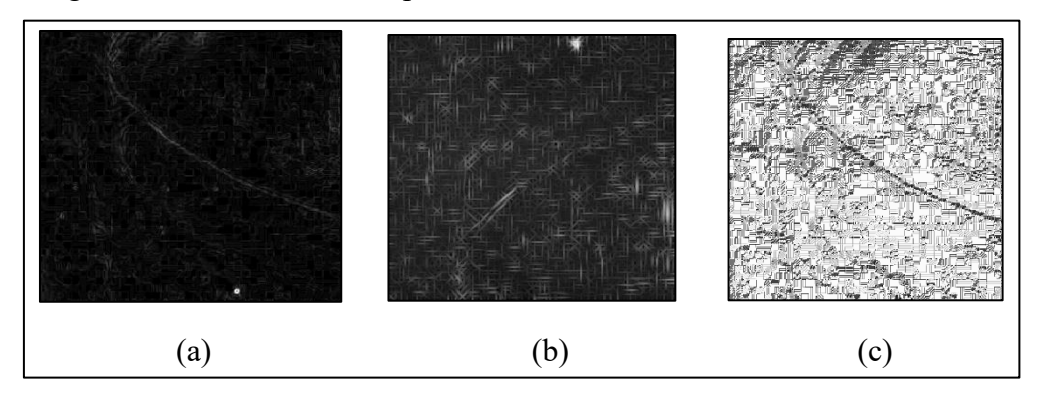


Figure 9. Palm Vein Processed ROI Applied with (a) HOG (b) Gabor (c) LBP

Classification performance is measured by overall accuracy and confusion matrices. Using multiple SVMs together improves accuracy and reliability in biometric systems, especially when there are changes in light, angle, and noise [40]. The majority voting method helps reduce errors and keeps results stable even when using different types of data. For palm vein recognition, using multiple SVMs aligns with past research on combining different biometric methods. This approach improves performance by using classifiers trained on different but related data of the same biometric feature. This is part of the proposed feature pipeline. Each descriptor  $f_k \in R^{d_k}$  where  $k \in \{HOG, LBP, Gabor\}$  captures distinct discriminatory cues: HOG encodes macro-structural vein flow orientation. LBP encodes finegrained texture and local contrast variations. Gabor encodes multi-scale, multi-directional frequency information for vein edge enhancement. For each feature type, an independent multiclass Support Vector Machine (SVM) classifier  $C_k$  is trained. Using the one-vs-one ECOC (Error-Correcting Output Codes) framework, the decision function for a test vector  $X_k$  is:

$$\widehat{y_{k}} = C_k(X_k) = \arg\max_{c \in \mathcal{Y}} w_c^T \phi(X_k) + b_c$$
 (20)

where  $\phi()$  is the linear kernel mapping,  $w_c$  and  $b_c$  are learned parameters, and y is the set of enrolled user identities. At inference time, the predictions from the three classifiers are fused using a majority voting scheme:

$$\hat{y} = mode(\{\hat{y}_{HOG}, \hat{y}_{LBP}, \hat{y}_{Gabor}\}) \tag{21}$$

Where *mode*() returns the most frequent label among the three predictions. This method combines different types of data to reduce errors. For example, if one type of data (like LBP) is affected by light changes, other types (like HOG and Gabor) can still make the right choice. If a user's test results are all wrong, a backup method called nearest neighbour (NN) search is used with a mixed data feature.

$$f_{hybrid} = [f_{HOG} | |f_{LBP}| | f_{Gabor}]$$
 (22)

The similarity between the query and training samples is computed using cosine distance:

$$d_{cos}(p,q) = 1 - \frac{p \cdot q}{||p||_2 \cdot ||q||_2}$$
 (23)

The label of the closest training sample is used as the final decision for that query. This setup ensures: Classifier diversity - different features notice different vein traits. Robustness to problems - if one feature does poorly, others make up for it. Fail-safe mechanism - backup NN matching stops complete failure for any user. For verification, cosine similarity on concatenated HOG, LBP and Gabor features was used; no classifier was trained. Images were pre-processed with CLAHE (clip=0.025), Gaussian smoothing ( $\sigma$ =0.5), resized to 300×300 (outer) and 150×150 (input). HOG used cell sizes {8,16,32} pixels, 9 bins; LBP radius=1, 8 neighbours, uniform, 32×32 cells; Gabor filters  $\lambda = \{4,8\}, \theta = \{0^{\circ},45^{\circ},90^{\circ},135^{\circ}\}$ , summarised by mean/std. Calibration for ECE/Brier used Platt-style logistic regression (IRLS, max 100 iters, tol=1e-6); fallback = min-max. Metrics include EER, TAR@10<sup>-3</sup>, AUC, with 95% CIs from 500 bootstraps. For the ensemble SVM, three linear SVMs (HOG, LBP, Gabor) were trained and fused by majority vote with NN fallback. Hyperparameters: linear kernel, C= {0.1,1,10} (final=1), kernel scale=auto, class weights balanced. Optimizer: SMO, maxIter=1e5, tol=1e-4. Model selection: 5-fold CV (normal condition) minimizing EER / maximizing TAR@10<sup>-3</sup>. Training data were augmented with small rotations ( $\pm 5^{\circ}$ ), translations ( $\pm 3$  pixels), and contrast jitter.

# 4.4 Feature Pipeline Comparison

Figure 10 compares the distribution of intra-class (genuine) and inter-class (impostor) similarity among the five conditions of acquisition across all four feature-extraction pipelines. The IUWT and Maximum Curvature methods demonstrate low levels of class separation, have overlapping distributions of scores and low genuine-impostor margin, which results in increased error rates. Gabor features are medium separable, intra-class scores show 0.70-0.75 clusters and inter-class scores show 0.80-0.85 clusters though there is still a significant overlap.

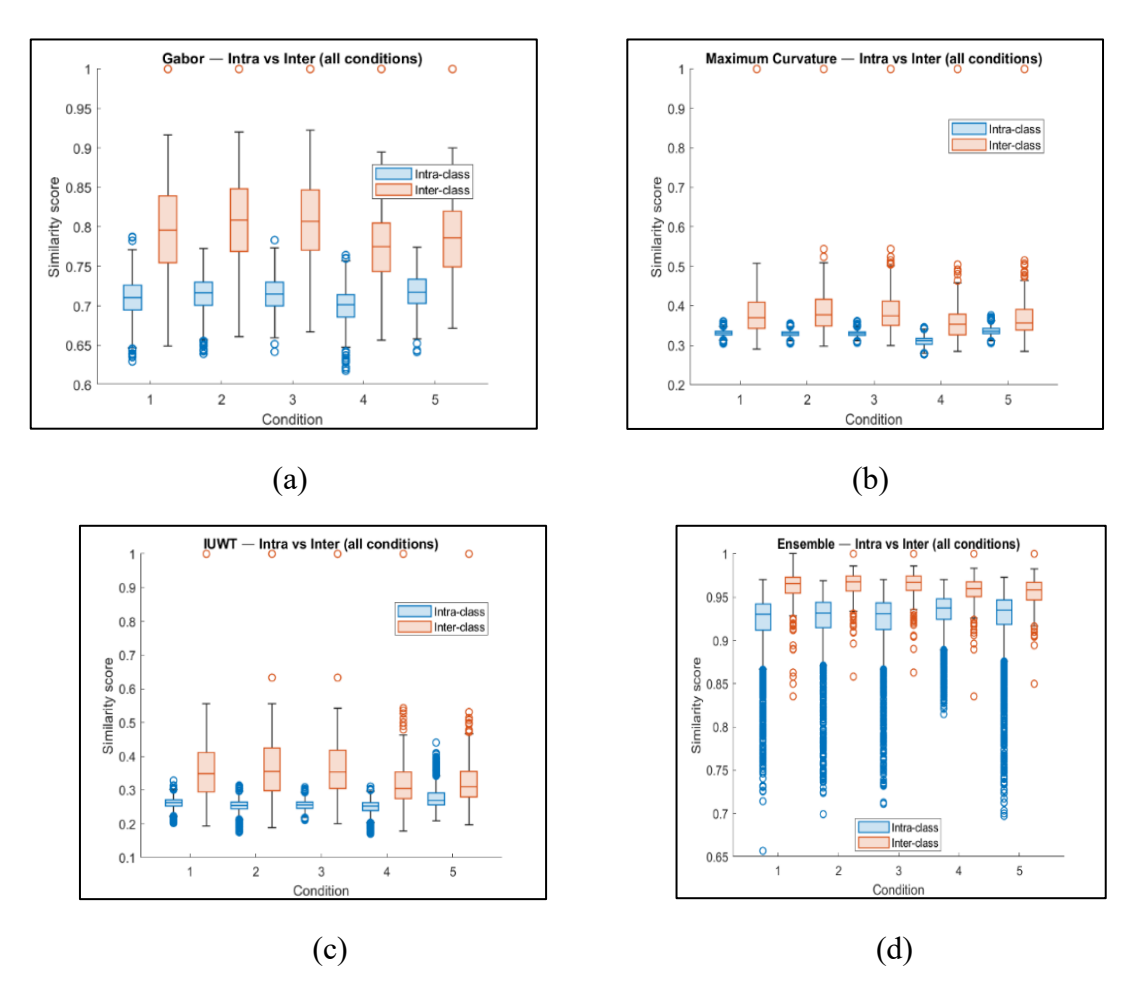


**Figure 10.** Inter and Intra Class Feature Distribution for (a) Kumar Gabor (b) Maximum Curvature (c) IUWT (d) Ensemble SVM Approach

The proposed ensemble of HOG, LBP and Gabor on the contrary, produces the most consistent and compact separation: intra-class scores are tightly clustered around 0.92-0.94, whereas inter-class scores are clustered around 0.96-0.97 across all conditions. Despite certain overlap that remains, the low variance and constant margins point to the enhanced strength of the ensemble approach. These distributions affirm the statistical tendencies in the EER and TAR measures and highlight the benefit of feature-level fusion to condition-robust palm vein recognition.

#### 5. Results

When comparing biometric verification, the FVC-type impostor protocol is a standardized testing method initially adopted by the Fingerprint Verification Competitions and thereafter used for other modalities such as palm vein authentication. If the dataset contains subjects, each with samples. The actual scores were calculated by verifying all different pairs of samples from the same person. The response of the verification system is evaluated using False Acceptance Rate (FMR) and the False Rejection Rate (FRR specified as:

$$FAR(\tau) = \frac{|\{s \in S_i : s \ge \tau\}|}{N_i}$$
 (24)

$$FRR(\tau) = \frac{|\{s \in S_g : s < \tau\}|}{N_g}$$
 (25)

here  $S_i$  and  $S_g$  represent impostor and genuine score sets respectively, s is the similarity score, and t is the decision threshold. The Equal Error Rate (EER) is the operating point where FAR(t)=FRR(t). Palm vein features were obtained from ROI images, and similarity scores were computed across the dataset. False acceptance rate (FAR) and false rejection rate (FRR) decision thresholds were obtained from the score distribution without specifically referring to subject-based pairs. Equal error rate (EER) and true acceptance rate (TAR) at a fixed FAR were obtained from these distributions. While such an "all-scores plug-in" approach shows initial separability, it can be deceptive as thresholds are dependent on the test set. In the final evaluation, FVC-type pairing regimes was employed where actual scores were obtained from within-subject tests and impostor scores from cross-subject tests. Every feature extraction technique was optimized for minimum EER, and decision thresholds were determined by scanning score values. EER was computed where FAR and FRR intersect, and TAR at target FAR (e.g., t) was computed likewise. Bootstrapped resampling was applied to estimate CIs for EER and TAR and provide more valid estimates than the all-scores method.

#### **5.1 Normalized cross-correlation (NCC)**

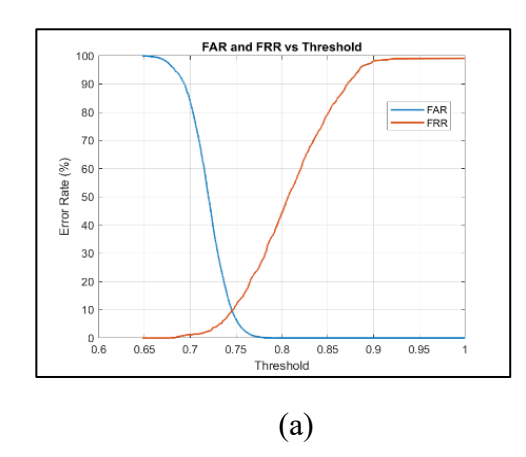
The Gabor magnitude response maps are normalized to reduce illumination bias and enhance local vein texture salience. Feature matching is done using normalized cross-correlation (NCC) between the probe and gallery corresponding Gabor magnitude maps [19]. The NCC score between two feature maps  $F_p$  and  $F_q$  is defined as:

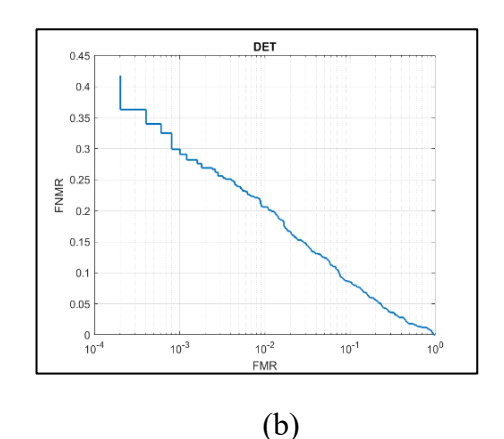
$$S_{NCC} = \frac{\sum_{x,y} (F_p(x,y) - \mu_p) (F_g(x,y) - \mu_g)}{\sqrt{\sum_{x,y} (F_p(x,y) - \mu_p)^2} * \sqrt{\sum_{x,y} (F_g(x,y) - \mu_g)^2}}$$
(26)

where  $\mu_p$  and  $\mu_g$  are the mean values of the probe and gallery feature maps. The final similarity score is computed as the average NCC value over all orientations:

$$S_{final = \frac{1}{N_{\theta}} \sum_{k=1}^{N_{\theta}} S(k)_{NCC}}$$
 (27)

A match is declared if  $S_{final}$  exceeds a decision threshold  $\tau$ , determined from training or validation data. Figure 11 shows the FAR, and FRR against the threshold curve, as well as the DET, ROC and conditions-wise curves.





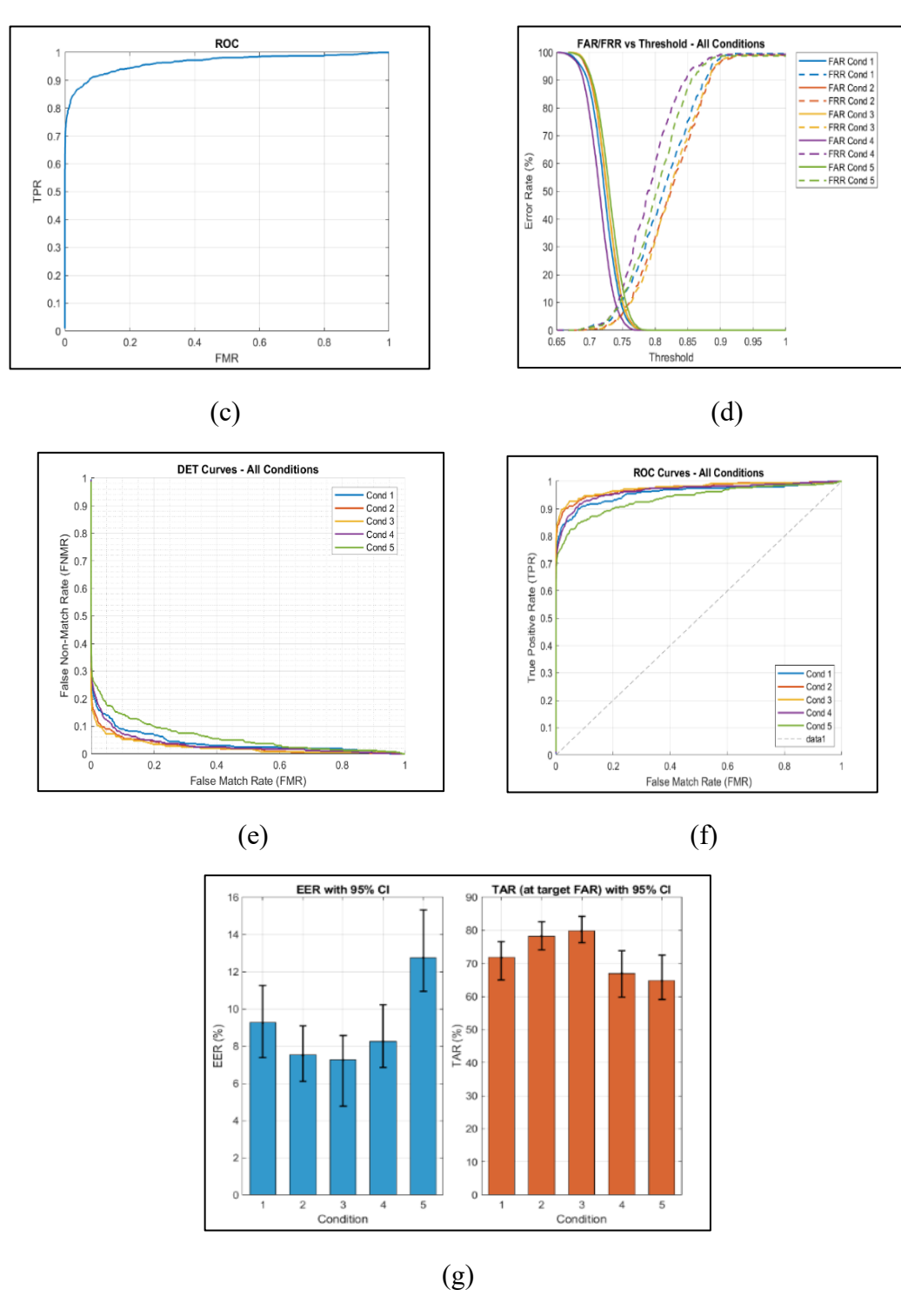


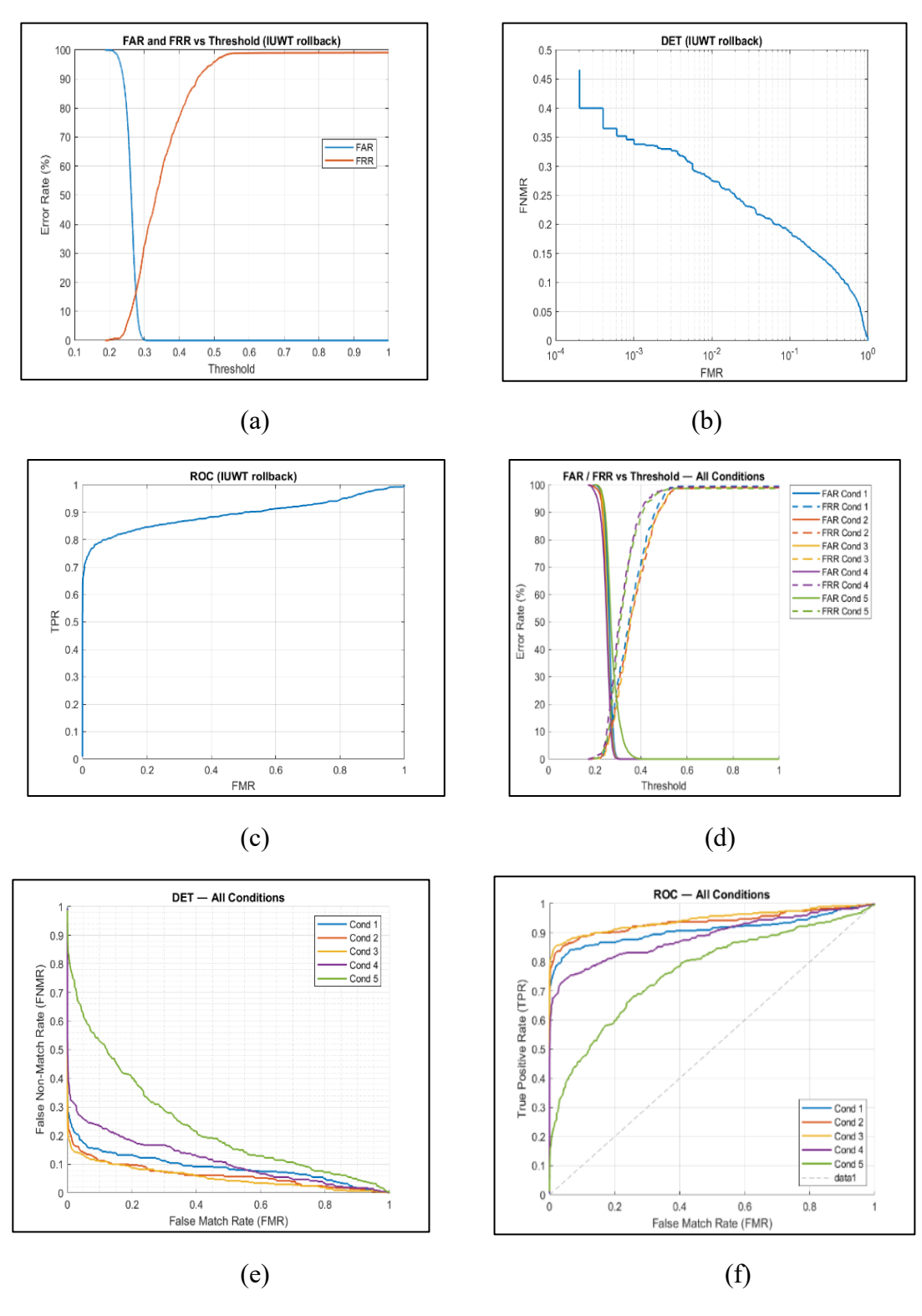
**Figure 11.** Kumar Gabor Approach (a) FAR, FRR (b) DET (c) ROC, Condition wise (d) FAR, FRR, (e) DET (f) ROC (g) EER, TAR with 95% CI

Kumar Gabor method resulted in fair recognition performance. The FAR–FRR and ROC curves show an EER of 8.8% with TAR of approximately 71% at FAR =  $10^{-3}$ , which demonstrates fair robustness against illumination change. The DET curve showed a balanced but non-optimal trade-off at more stringent thresholds. Genuine–impostor score distributions had partial overlap, but with reasonably discriminative clusters. Condition-wise distributions demonstrated that temperature fluctuations (hot, cold) have little effect, whereas surface

impurities (dust, lotion) decreased margins of separation more significantly. Calibration plots were stable (low ECE and Brier), affirming uniform confidence estimates.

# 5.2 Sum of Absolute Differences (SAD)

The scale-specific detail coefficients from IUWT are normalized to reduce sensitivity to illumination changes and combined into a unique feature vector.



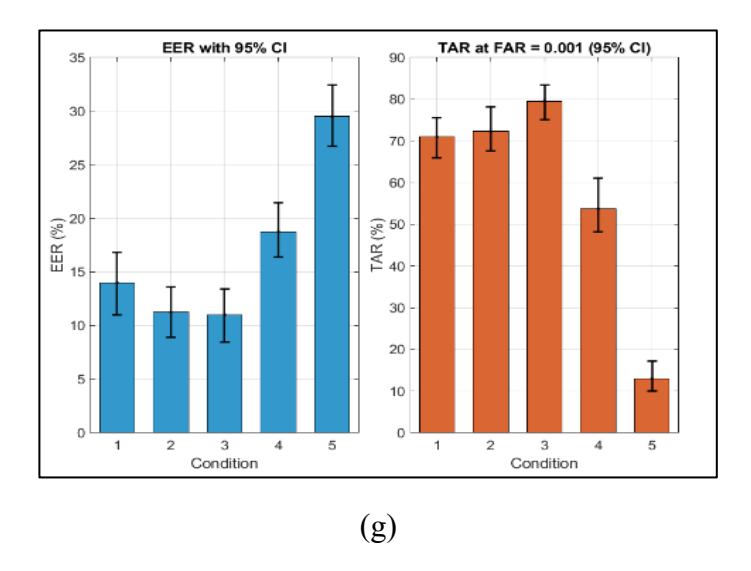


**Figure 12.** IUWT Approach (a) FAR, FRR (b) DET (c) ROC, Condition wise (d) FAR, FRR, (e) DET (f) ROC (g) EER, TAR with 95% CI

Sum of absolute differences (SAD) is utilized for matching, an L1-norm distance metric between the probe  $f_p$  and  $f_g$  feature vectors:

$$d_{L1}(f_p, f_q) = \sum_{i=1}^n |f_{p,i} - f_{q,i}|$$
(28)

A lower  $d_{L1}$  value indicates greater resemblance between the two feature vectors. Verification decisions follow the rule Match if  $d_{L1} \le \tau$ .  $\tau$  is decision threshold, empirically determined from training or validation data. Figure 12 shows the FAR, FRR against threshold curve, DET, ROC and conditions wise curves. The IUWT-SAD procedure had the poorest robustness. FAR–FRR and ROC plots yielded an EER of 16.4% with TAR as low as 62%, suggesting low discrimination. DET plots were extremely unreliable, particularly at low values of FAR. Genuine–impostor score distributions suggested heavy overlap under all circumstances. Condition-by-condition analysis further emphasized this flaw: both temperature changes and surface effects significantly reduce separability with lotion causing the largest performance degradation. Despite this, calibration values were within reasonable limits, meaning that decision scores are discriminative but not well-scaled.

#### **5.3 Pointwise Correlation Matching**

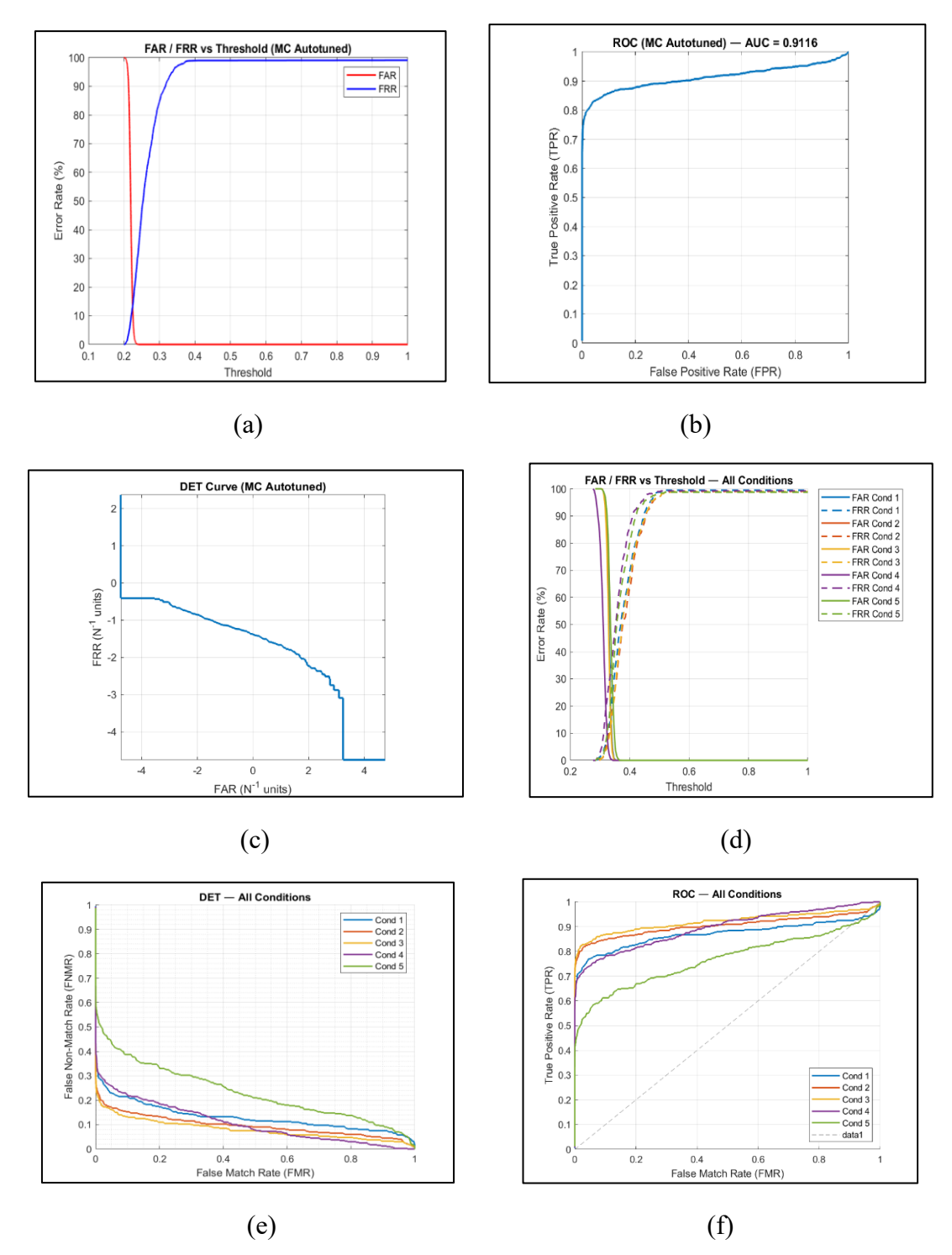
The MC algorithm detects vessel centrelines by computing curvature along intensity cross-sections and picking the points of maximum negative curvature. The result is a binary vein pattern map. Since hand placement can vary slightly, the probe and gallery templates are shifted in x and y within a small search range ( $\pm t_{max}$ ) pixels. Normalized Cross-Correlation Matching computes, for each translation (u, v),

$$S_{(u,v)=\frac{\sum_{x,y}(V_p(x,y).V_g(x+u,y+v)}{\sqrt{\sum_{x,y}(V_p(x,y)^2},\sqrt{\sum_{x,y}V_g(x+u,y+v)^2}}}$$
(29)

where  $V_p$  is the probe vein map,  $V_g$  is the gallery vein map, and the sums run over the overlapping region after the shift. The maximum correlation over all translations is taken as the similarity score.

$$S_{final} = \max_{u,v} S(u,v) \tag{30}$$

Verification decisions follow the rule Match if  $S_{final} \ge \tau$ . The Figure 13 shows the FAR, FRR against threshold curve, DET, ROC and conditions wise curves.



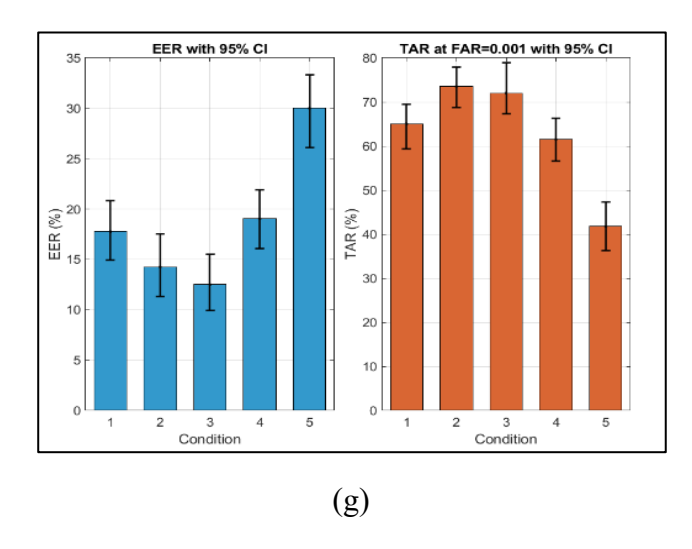
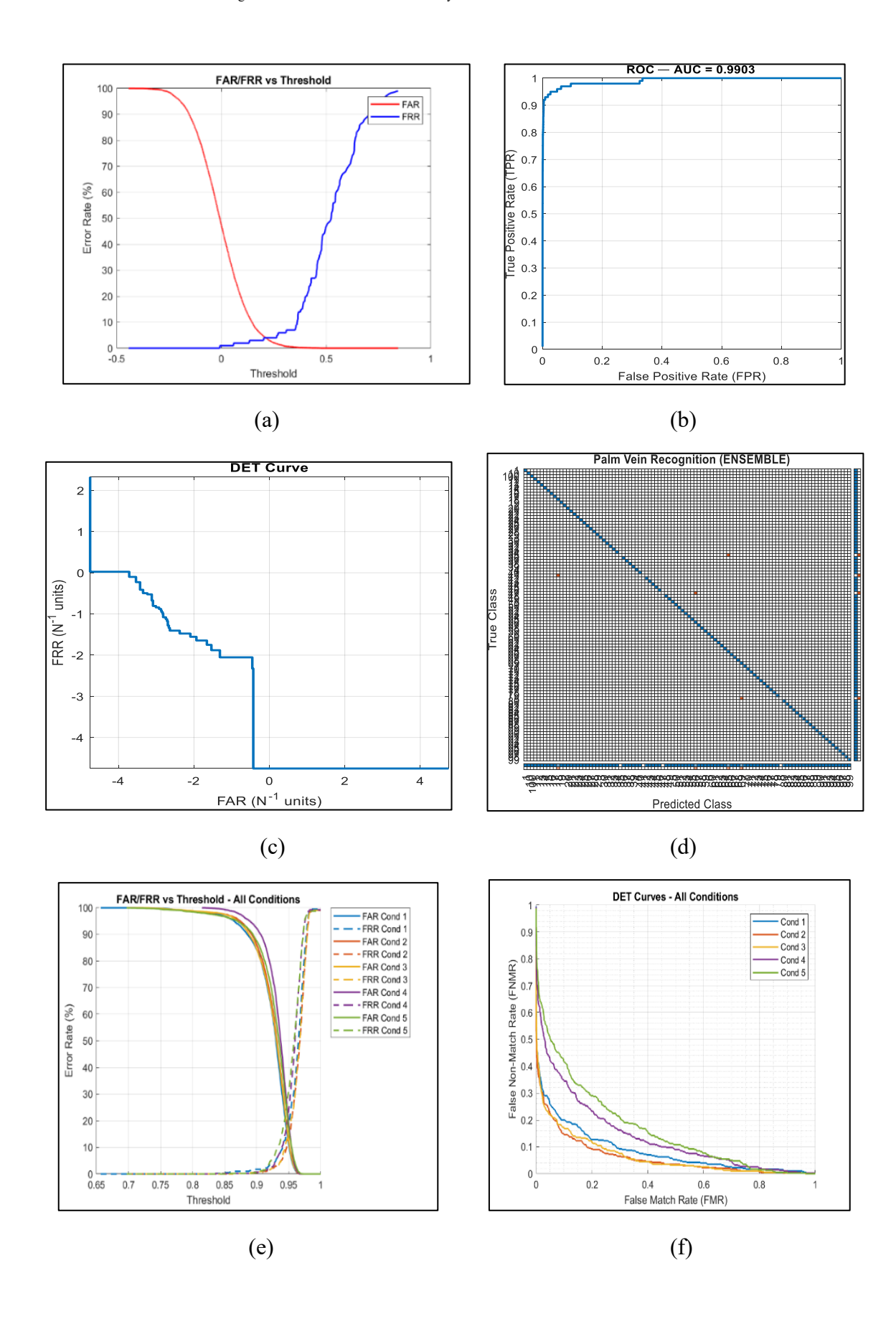


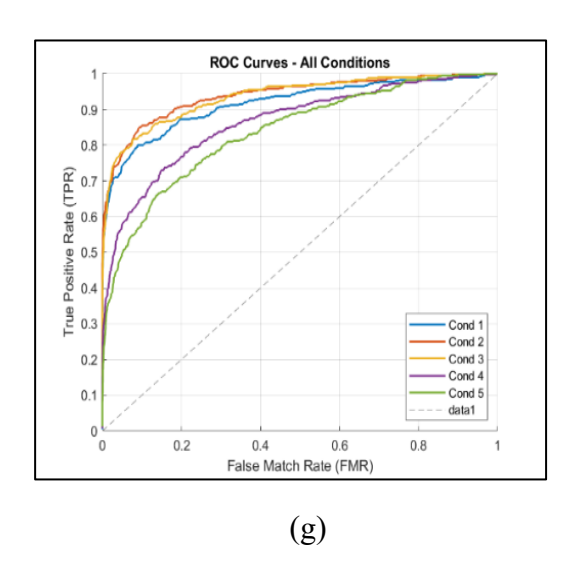
**Figure 13.** MC Approach (a) FAR, FRR (b) DET (c) ROC, Condition wise (d) FAR, FRR, (e) DET (f) ROC (g) EER, TAR with 95% CI

The Maximum Curvature algorithm performed midway between IUWT and Gabor. FAR–FRR and ROC plots yielded an EER of 13.1% and a TAR of around 66%, exhibiting partial robustness. DET curves showed increasing FRR at tighter operating points, confirming sensitivity under tight impostor thresholds. Score distributions showed only modest separation, with considerable overlap remaining. Condition-wise distributions indicated relative stability under hot/cold variations but a drastic decline under dust and lotion conditions where separability is less. Calibration errors were still low, indicating stable probability estimates even as discrimination power declined.

## 5.4 Handcrafted Multi-Feature Ensemble with SVM Classification

Here, discriminative feature vectors are extracted from palm vein ROI images using a combination of Histogram of Oriented Gradients (HOG), Local Binary Patterns (LBP), and Gabor filter responses. These feature vectors were used to train a multi-class Support Vector Machine (SVM) classifier in a one-vs-one scheme. During testing, the classifier produced predicted labels for unseen samples, which were compared against the true class identities to generate similarity scores. From these scores, genuine match distributions (comparisons between samples of the same subject) were constructed and impostor match distributions (comparisons across different subjects). The False Acceptance Rate (FAR) was computed as the fraction of impostor comparisons incorrectly classified as genuine, while the False Rejection Rate (FRR) was computed as the fraction of genuine comparisons incorrectly classified as impostors.





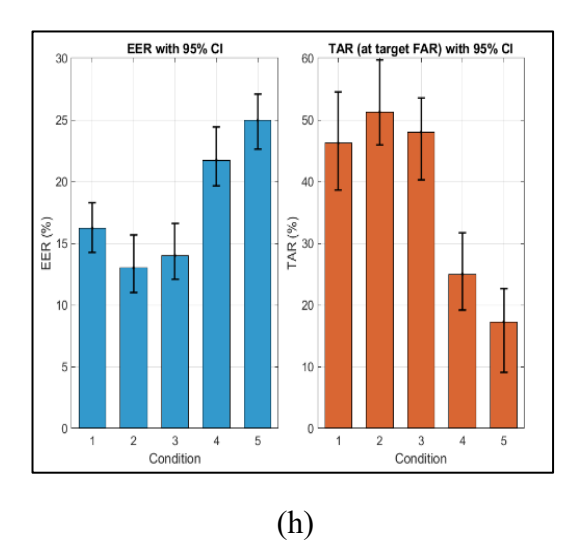


**Figure 14.** Ensemble SVM Approach a) FAR, FRR (b) DET (c) ROC, (d) Confusion Matrix Condition wise (e) FAR, FRR, (f) DET (g) ROC (h) EER, TAR with 95% CI

Figure 14 shows the FAR and FRR against the threshold curve, DET, ROC and conditions wise curves. The ensemble SVM achieves the strongest results across analyses. The FAR-FRR and ROC curves show the lowest EER of 4.0% and the highest TAR (72.3% at FAR =  $10^{-3}$ ). DET curves confirm robustness across the operating range, unlike single-feature methods. Genuine-impostor distributions show minimal overlap, demonstrating strong discrimination. The condition-wise plots demonstrate stability under hot and cold conditions, and while dust and lotion reduce margins, clusters remain well separated.

Calibration analysis (ECE  $\leq 0.02$ , Brier  $\leq 0.03$ ) validated reliable confidence scores, confirming the ensemble as the most robust pipeline. A more detailed per-condition calibration analysis showed that errors remained consistently low across environmental shifts. Relative to the normal baseline (ECE = 0.0054, Brier = 0.0187), the cold and hot conditions increased ECE by +0.0086 and +0.0092 respectively, while slightly improving Brier (-0.0035 and -0.0048). Under dusty and lotion conditions, ECE rose by +0.0145 and +0.0111, with Brier worsening by +0.0051 and +0.0052. Importantly, all calibration errors stayed <0.025, confirming that even under contaminants the model's confidence estimates remained reliable. Analysis showed stability under temperature variations, with TAR@10<sup>-3</sup> reaching 78.3% in cold and 79.8% in hot conditions, and EERs below 8%. Surface contamination posed challenges: TAR dropped to 67.0% (EER 8.3%) under dust and 64.8% (EER 12.8%) under lotion. The normal baseline achieved 71.8% TAR with 9.3% EER. AUC remained above 0.93 and calibration error (ECE < 0.02, Brier < 0.03) stayed low, showing reliable decision confidence across conditions. Table 2 further compares the four feature-extraction pipelines. IUWT-SAD showed the weakest performance (EER 16.4%, TAR 62%), followed by Maximum Curvature (EER 13.1%, TAR 66%), while Kumar Gabor achieved moderate robustness (EER 8.8%, TAR 71%). The proposed ensemble SVM provided the best trade-off, with an average EER of 4.0%, TAR@10<sup>-3</sup> of 72.3%, and the highest AUC (0.963). In terms of efficiency, throughput ranged from 7.8 to 9.5 images/second, with the ensemble operating near the upper end. These findings demonstrate that while single-feature pipelines degrade under challenging conditions, ensemble fusion substantially improves robustness and achieves a validated balance of accuracy, calibration, and computational feasibility.

**Table 2.** Comparison of Feature-Extraction Pipelines across Accuracy, Calibration, Efficiency, and Memory Metrics

Method	Avera ge EER (%)	Averag e TAR@ 1e <sup>-3</sup> (%)	Avera ge AUC	Avera ge ECE	Avera ge Brier	Average Throughp ut (image/s)	Featur e Storag e (MB)	MATLA B Mem Used (MB)
Gabor-NCC	8.8	71	0.95	0.012	0.02	9.5	3.9	5183
IUWT-SAD	16.4	62	0.91	0.018	0.027	8	4	5183
Maximum Curvature	13.13	66	0.93	0.016	0.024	7.8	4.2	5183
Ensemble SVM (proposed)	4	72.3	0.963	0.014	0.019	8.8	4.2	5183

Feature storage across all pipelines remained modest (3.9–4.2 MB), and MATLAB runtime memory usage was consistent at ~5.2 GB, indicating that even the proposed ensemble remains lightweight compared to typical deep learning models. This confirms that the method is feasible for deployment in resource-constrained or embedded environments. To evaluate the effect of individual preprocessing blocks on recognition performance, a controlled ablation study across four pipelines (Ensemble SVM, Gabor, Maximum Curvature, and IUWT) was conducted. Specifically, contrast enhancement (No CLAHE), denoising (No Gaussian smoothing), and vein map extraction (using raw intensities or reduced feature sets) were disabled while keeping the remaining pipeline unchanged. Table 3 evaluates the contribution of individual preprocessing stages across the four pipelines. The results confirm that contrast enhancement (CLAHE) is essential: removing it nearly doubled the EER for IUWT (12.1%  $\rightarrow$ 26.5%) and tripled the error for Ensemble (13.7%  $\rightarrow$  39.3%). In contrast, denoising had only a marginal influence (<1-2% change in EER for Gabor, MC, and IUWT), suggesting that Gaussian filtering plays a secondary role compared to contrast normalization. The most severe degradation was observed when vein map extraction was disabled, with EER increasing from 14.8% to 28.2% for MC and from 12.1% to 33.9% for IUWT. Even the Ensemble "raw-only" variant reached 35.1% EER, highlighting the necessity of explicit vein enhancement and feature fusion. Overall, the ablation study validates the design choices of the proposed pipeline: CLAHE ensures robustness to condition-induced contrast changes, vein extraction provides discriminative structure, and the combination of HOG, LBP, and Gabor features yields the most reliable recognition performance.

Table 3. Ablation Study of Preprocessing Steps

Pipeline	Variant	EER (%)	Threshold
Gabor	Full Pipeline	7.72	0.758
	No CLAHE	7.5	0.768
	No Denoise	7.72	0.76

	No Vein Extract	13.42	0.576
MC	Full Pipeline	14.8	0.357
	No CLAHE	17.1	0.346
	No Denoise	15	0.35
	No Vein Extract	28.2	0.464
IUWT	Full Pipeline	12.1	0.283
	No CLAHE	26.5	0.236
	No Denoise	12.3	0.283
	No Vein Extract	33.9	0.791
Ensemble	Full Pipeline	13.68	0.916
	No CLAHE	39.28	0.9
	No Denoise	25.31	0.951
	No Vein Extract A (HOG+LBP only)	13.68	0.916
	No Vein Extract B (Gabor only)	30	0.992
	No Vein Extract C (Raw only)	35.09	0.986

It is important to note that the absolute EER values in Table 3 are not directly comparable to those in Table 2. The main results in Table 2 were obtained using the full verification/classification pipeline with calibration and subject-level splits, whereas the ablation study in Table 3 was performed under a simplified pairwise cosine verification setting to isolate the effect of individual preprocessing blocks. This protocol change naturally yields higher EERs in Table 3, particularly for the ensemble variant. However, the relative trends remain consistent across both tables: contrast enhancement (CLAHE) and vein extraction are indispensable, denoising has minimal impact, and ROI alignment is critical for reproducibility.

#### 6. Conclusion

The work presented a condition-robust palm vein dataset consisting from 500 palm vein images of 100 subjects, which were collected in five real-world environmental conditions (normal, hot, cold, dusty and lotion-applied). Based on this dataset, a systematic comparison of various existing feature extraction pipelines (Kumar Gabor, IUWT-SAD, Maximum Curvature) is made, along with a new proposed multi-feature ensemble SVM which integrates HOG, LBP and Gabor descriptors. The suggested ensemble performed systematically better than single pipelines, attaining the lowest EER (4.0%), the highest TAR (72.3% at FAR=10-3), and the best calibration (AUC = 0.963, ECE < 0.02, Brier < 0.03). Notably, it was robust

against environmental stress (temperature change, contamination of the surface). An ablation study further highlighted the role of preprocessing. Removing contrast enhancement (CLAHE) led to sharp performance drops across all pipelines (e.g., Ensemble:  $13.7\% \rightarrow 39.3\%$  EER; IUWT:  $12.1\% \rightarrow 26.5\%$  EER), while removing vein map extraction caused the most severe degradation (up to 34% EER for IUWT). In contrast, denoising had a negligible effect. These findings confirm that CLAHE and explicit vein enhancement are indispensable for robust recognition, while feature fusion in the ensemble maximizes discriminative power. The efficiency analysis proved that the algorithm is computationally light, with a throughput of approximately 9-12 images per second on commodity hardware, memory footprint of less than 5.2GB and feature storage of less than 5MB. The method has been shown to be effective in embedded biometric applications.

Besides the new dataset, this work demonstrates that manually constructed feature collections are still highly useful for condition-robust biometric recognition, particularly in cases where large-scale deep learning is inapplicable due to data or resource constraints. There are still some limitations. The size of the dataset, while sufficient to accomplish the analysis of controlled conditions, is limited to one demographic (students aged 18-20). Inter-dataset validation over publicly available benchmarks (PolyU, VERA, etc.) and ablation of preprocessing components (denoising, ROI alignment, contrast enhancement) were not performed because of scope limitations. Nevertheless, they are both clearly labeled possible future research directions, as well as expansion of the datasets and inclusion of more modern deep learning frameworks to expand their generalization. In summary, the work has the following contributions (i) a new reference dataset has been explicitly created to challenge robustness in the presence of realistic acquisition variability, and (ii) a lightweight, tested ensemble method has been explicitly developed that exhibits high recognition accuracy, calibration and efficiency. The results provide a solid foundation for the further development of condition-robust palm vein recognition and emphasize the potential for practical implementation beyond laboratory conditions.

#### References

- [1] Wu, Wei, Stephen John Elliott, Sen Lin, Shenshen Sun, and Yandong Tang. "Review of palm vein recognition." IET Biometrics 9, no. 1 (2020): 1-10.
- [2] Rastogi, Swati, Siddhartha P. Duttagupta, Anirban Guha, and Surya Prakash. "Palm vein pattern: Extraction and Authentication." In 2020 IEEE International Conference on Machine Learning and Applied Network Technologies (ICMLANT), IEEE, (2020): 1-5.
- [3] Wu, Wei, Yunpeng Li, Yuan Zhang, and Chuanyang Li. "Identity recognition system based on multi-spectral palm vein image." Electronics 12, no. 16 (2023): 3503.
- [4] Htet, Aung Si Min, and Hyo Jong Lee. "Contactless palm vein recognition based on attention-gated residual U-Net and ECA-ResNet." Applied Sciences 13, no. 11 (2023): 6363.
- [5] Hernández-García, Ruber, Ricardo J. Barrientos, Cristofher Rojas, and Marco Mora. "Individuals identification based on palm vein matching under a parallel environment." Applied Sciences 9, no. 14 (2019): 2805.

- [6] Kauba, Christof, and Andreas Uhl. "Robustness evaluation of hand vein recognition systems." In 2015 International Conference of the Biometrics Special Interest Group (BIOSIG), IEEE, (2015): 1-5.
- [7] Uhl, Andreas, Christoph Busch, Sébastien Marcel, and Raymond Veldhuis. Handbook of vascular biometrics. Springer Nature, 2020.
- [8] Gu, Kim Seung, Kim Jung Soo, and Park Kang Ryoung. "FGFNet: Fourier Gated Feature-Fusion Network with Fractal Dimension Estimation for Robust Palm-Vein Spoof Detection." Fractal and Fractional 9, no. 8 (2025): 478.
- [9] He, Zheng, Qiantong Xu, Yapeng Ye, and Wenxin Li. "Effects of meteorological factors on finger vein recognition." In 2017 IEEE International Conference on Identity, Security and Behavior Analysis (ISBA), (IEEE, 2017): 1-8.
- [10] Al-Khafaji, Ruaa SS, and Mohammed SH Al-Tamimi. "Vein biometric recognition methods and systems: A review." Advances in Science and Technology. Research Journal 16, no. 1 (2022): 36-46.
- [11] Hemis, Mustapha, Hamza Kheddar, Sami Bourouis, and Nasir Saleem. "Deep learning techniques for hand vein biometrics: A comprehensive review." Information Fusion 114 (2025): 102716.
- [12] Chen, Yung-Yao, Chih-Hsien Hsia, and Ping-Han Chen. "Contactless multispectral palm-vein recognition with lightweight convolutional neural network." IEEE Access 9 (2021): 149796-149806.
- [13] Ruan, Lihua, Zhiqin Yin, Shibing Zhou, Weibo Zheng, Wei Lu, Tao Zhang, and Shaowei Wang. "Vein visualization enhancement by dual-wavelength phase-locked denoising technology." Journal of Innovative Optical Health Sciences 17, no. 03 (2024): 2350033.
- [14] Dai, Fen, Ziyang Wang, Xiangqun Zou, Rongwen Zhang, and Xiaoling Deng. "Noncontact palm vein ROI extraction based on improved lightweight HRnet in complex backgrounds." IET Biometrics 2024, no. 1 (2024): 4924184.
- [15] Kuang, Ying, Shuai Wang, Bincheng Mo, Shiyou Sun, Kai Xia, and Yuanmu Yang. "Palm vein imaging using a polarization-selective metalens with wide field-of-view and extended depth-of-field." npj Nanophotonics 1, no. 1 (2024): 24.
- [16] Mohamed, Abdelnasser, Ahmed Salama, and Amr Ismail. "Enhancing Ad Hoc Network Security using Palm Vein Biometric Features." Engineering, Technology & Applied Science Research 15, no. 1 (2025): 20034-20041.
- [17] Ozkan, Haydar, Muberra Aydin, Osman Ozcan, and Ümmühan Zengin. "A portable multispectral vein imaging system." Journal of Electrical Engineering 74, no. 1 (2023).
- [18] Lou, Jiashu, and Baohua Wang. "Palm vein recognition via multi-task loss function and attention layer." arXiv preprint arXiv:2211.05970 (2022).
- [19] Kumar, Ajay, and Yingbo Zhou. "Human identification using finger images." IEEE Transactions on image processing 21, no. 4 (2011): 2228-2244.

- [20] Aqreerah, Salwua, Alhaam Alariyibi, and Wafa El-Tarhouni. "Multispectral palmprint recognition based on three descriptors: LBP, Shift LBP, and Multi Shift LBP with LDA classifier." In 2022 IEEE 2nd International Maghreb Meeting of the Conference on Sciences and Techniques of Automatic Control and Computer Engineering (MI-STA), IEEE, (2022): 506-510
- [21] Yang, Yang, Yingyue Zhou, Runxia Huang, Qi Liu, Hongsen He, and Xiaoxia Li. "Contactless Palmprint and Palm Vein Identity Recognition Via a Bimodal Network with Parameter-Adaptive Log-Gabor Convolution." Available at SSRN 4625638.
- [22] Wu, Wei, Yuan Zhang, Yunpeng Li, and Chuanyang Li. "Fusion recognition of palmprint and palm vein based on modal correlation." Mathematical Biosciences and Engineering 21, no. 2 (2024): 3129-3145.
- [23] Fanjiang, Yong-Yi, Cheng-Chi Lee, Yan-Ta Du, and Shi-Jinn Horng. "Palm vein recognition based on convolutional neural network." Informatica 32, no. 4 (2021): 687-708.
- [24] Li, Meihui, Yufei Gong, and Zhaohui Zheng. "Finger vein identification based on large kernel convolution and attention mechanism." Sensors 24, no. 4 (2024): 1132.
- [25] Albano, Rocco, Lorenzo Giusti, Emanuele Maiorana, and Patrizio Campisi. "Explainable vision transformers for vein biometric recognition." IEEE Access 12 (2024): 60436-60446.
- [26] Wulandari, Meirista, Rifai Chai, Basari Basari, and Dadang Gunawan. "Hybrid Feature Extractor Using Discrete Wavelet Transform and Histogram of Oriented Gradient on Convolutional-Neural-Network-Based Palm Vein Recognition." Sensors 24, no. 2 (2024): 341.
- [27] Zhang, Renye, Yimin Yin, Wanxia Deng, Chen Li, and Jinghua Zhang. "Deep learning for finger vein recognition: A brief survey of recent trend." arXiv preprint arXiv:2207.02148 (2022).
- [28] Qin, Huafeng, Yuming Fu, Jing Chen, Mounim A. El-Yacoubi, Xinbo Gao, and Feng Xi. "Neural architecture search based global-local vision mamba for palm-vein recognition." arXiv preprint arXiv:2408.05743 (2024).
- [29] Jin, Xin, Hongyu Zhu, Mounîm A. El Yacoubi, Haiyang Li, Hongchao Liao, Huafeng Qin, and Yun Jiang. "Starlknet: Star mixup with large kernel networks for palm vein identification." arXiv preprint arXiv:2405.12721 (2024).
- [30] Shang, Sheng, Chenglong Zhao, Ruixin Zhang, Jianlong Jin, Jingyun Zhang, Rizen Guo, Shouhong Ding, Yunsheng Wu, Yang Zhao, and Wei Jia. "PVTree: Realistic and Controllable Palm Vein Generation for Recognition Tasks." In Proceedings of the AAAI Conference on Artificial Intelligence, vol. 39, no. 7, (2025): 6767-6775.
- [31] Qin, Huafeng, Yuming Fu, Huiyan Zhang, Mounim A. El-Yacoubi, Xinbo Gao, Qun Song, and Jun Wang. "MsMemoryGAN: A Multi-scale Memory GAN for Palm-vein Adversarial Purification." arXiv preprint arXiv:2408.10694 (2024).

- [32] Chen, Liukui, Tengwen Guo, Li Li, Haiyang Jiang, Wenfu Luo, and Zuojin Li. "A finger vein liveness detection system based on multi-scale spatial-temporal map and light-vit model." Sensors 23, no. 24 (2023): 9637.
- [33] Chate, Suhas, Vijay Patil, and Yuvraj Parkale. "A Novel Setup for Palm Vein Biometrics Database Collection Under Different External Conditions." In 2024 2nd International Conference on Signal Processing, Communication, Power and Embedded System (SCOPES), IEEE, (2024): 1-6.
- [34] Kirchgasser, Simon, Christof Kauba, and Andreas Uhl. "Towards Understanding Acquisition Conditions Influencing Finger Vein Recognition." In Handbook of vascular biometrics, Cham: Springer International Publishing, (2019): 179-199.
- [35] Moroń, Tomasz, Krzysztof Bernacki, Jerzy Fiołka, Jia Peng, and Adam Popowicz. "Recognition of the finger vascular system using multi-wavelength imaging." IET Biometrics 11, no. 3 (2022): 249-259.
- [36] Wang, Haixia, Lixun Su, Hongxiang Zeng, Peng Chen, Ronghua Liang, and Yilong Zhang. "Anti-spoofing study on palm biometric features." Expert Systems with Applications 218 (2023): 119546.
- [37] Kauba, Christof, and Andreas Uhl. "An available open-source vein recognition framework." In Handbook of Vascular Biometrics, pp. 113-142. Cham: Springer International Publishing, 2019.
- [38] Genovese, Angelo, Vincenzo Piuri, Konstantinos N. Plataniotis, and Fabio Scotti. "PalmNet: Gabor-PCA convolutional networks for touchless palmprint recognition." IEEE Transactions on Information Forensics and Security 14, no. 12 (2019): 3160-3174.
- [39] Zhou, Yingbo, and Ajay Kumar. "Human identification using palm-vein images." IEEE transactions on information forensics and security 6, no. 4 (2011): 1259-1274.
- [40] Abukmeil, Y. R., and G. L. Marcialis. 2020. "Experimental Results on Palm Vein Based Personal Recognition Using Multi-Snapshot Fusion of Textural Features." arXiv Preprint arXiv:2008.11818.